Seasonal variations in the South Atlantic Meridional Overturning Circulation from observations and numerical models

Shenfu Dong[1,2], Molly O. Baringer[2], Gustavo J. Goni[2], Christopher S. Meinen[2], and Silvia L. Garzoli[1,2]

[1]CIMAS, University of Miami, Miami, Florida, USA, [2]AOML, NOAA, Miami, Florida, USA

Abstract Monthly climatologies of temperature and salinity from observations and numerical models are used to estimate the Atlantic Meridional Overturning Circulation (AMOC) at 34°S. Observational estimates suggest that the geostrophic transport plays an equal role to the Ekman transport in the AMOC seasonal variations at this latitude, whereas in the models, the Ekman transport controls the AMOC seasonality. The seasonality of the geostrophic transport from observations is largely controlled by the seasonal density variations at the western boundary, but in the models, the eastern boundary dominates. The observed density seasonality at the western boundary is linked to the intensity of the Malvinas Current, which is poorly reproduced in the models. The results indicate that the weak seasonal cycle in the model geostrophic transport can primarily be attributed to excessively strong baroclinicity below the surface mixed layer, whereas the observations show a strong vertical coherence in the velocity down to 1200 m.

1. Introduction

The Atlantic Meridional Overturning Circulation (AMOC), as the main route for the global ocean heat conveyor belt circulation, can have a direct and pronounced impact on a variety of climate phenomena, such as African and Indian monsoon rainfall and hurricane activity in the North Atlantic sector [e.g., *Vellinga and Wood*, 2002; *Zhang and Delworth*, 2006]. Our current understanding of the AMOC and its governing mechanisms depends heavily on the use of numerical models due to limited direct observations; these model-based studies [e.g., *Thorpe et al.*, 2001; *Stouffer et al.*, 2006; *Smith and Gregory*, 2009] have provided important insights into AMOC behavior, but the value of those insights is dependent on the fidelity of the models to the real world. In order to assess the climate impact of the AMOC and predict future climate change, it is important that climate models accurately simulate changes in the AMOC in response to forcing.

Observations from both the North and South Atlantic suggest that the geostrophic contribution to the strength of the maximum meridional volume transport by the AMOC (referred to as AMOC hereafter) and the total meridional heat transport (MHT) plays an equal or more important role compared to that played by the Ekman transport in terms of the total AMOC and MHT seasonal to interannual variability [e.g., *Kanzow et al.*, 2009; *Johns et al.*, 2011; *Dong et al.*, 2009, 2011; *McCarthy et al.*, 2012]. However, studies based on numerical models [e.g., *Böning et al.*, 2001; *Jayne and Marotzke*, 2001; *Baringer et al.*, 2013; *Msadek et al.*, 2013] indicate that the seasonal to interannual variations in the AMOC and MHT are predominately controlled by the Ekman term. These differences between numerical models and observations suggest that the AMOC and MHT in models may respond to forcing differently than in the real ocean. Therefore, it is crucial to evaluate and diagnose what causes the differences seen in the AMOC and MHT between observational based estimates and model simulations in order to improve numerical models. In this study, we focus on 34°S in the South Atlantic, where a repeated high-density expendable bathythermograph (XBT) transect has provided the first quarterly time series of the AMOC and MHT in the South Atlantic since 2002, from which the observed seasonal cycle can been estimated [*Garzoli and Baringer*, 2007; *Dong et al.*, 2009; *Garzoli et al.*, 2013]. Note that although only the AMOC is discussed in this paper, the results obtained here also apply to the MHT, because changes in the MHT are strongly correlated with changes in the AMOC [*Dong et al.*, 2009; *Johns et al.*, 2011]. The main objective of this study is to investigate what causes the differences in the AMOC seasonal variations estimated from observations and numerical models.

2. Data and Methodology

Monthly climatologies of temperature and salinity (*T/S*) on a 1° longitude grid along 34°S are constructed both from observations and numerical models to estimate the AMOC. The observational *T/S* climatology is

mainly derived from gridded Argo T/S monthly fields from 2004 to 2013 [*Roemmich and Gilson*, 2009], which provide data from the sea surface down to ~2000 m depth. The T/S monthly climatology from the World Ocean Atlas 2013 (WOA13) [*Locarnini et al.*, 2013] is padded below the Argo depth to construct the full depth profiles. Two widely used coupled climate models, National Center for Atmospheric Research Community Climate System Model version 4 (CCSM4) [e.g., *Gent et al.*, 2011; *Danabasoglu et al.*, 2012] and the Geophysical Fluid Dynamics Laboratory–Earth System Model (GFDL-ESM2M) [e.g., *Dunne et al.*, 2012; *Parsons et al.*, 2014] twentieth century run from Coupled Model Intercomparison Project phase 5 (CMIP5), are examined in this study. The last 50 years of the model output is used to derive the T/S monthly climatology. There are 60 vertical layers in CCSM4 and 50 vertical layers in GFDL-ESM2M. The T/S fields from Argo/WOA13 are interpolated to the same 60 vertical layers of CCSM4. Note that Argo floats are unable to reliably sample regions, where the ocean bottom is shallower than 1000 m, resulting in one grid point near each boundary that is not well sampled. To address this, T/S from WOA13 are used in these two grid locations. The analysis of the existing data indicates that the net volume transport through these two grid points is less than 0.3 sverdrup (Sv), which is roughly an order of magnitude smaller than the total MOC and its seasonal variations.

Geostrophic velocity is computed from the thermal wind relationship with the reference level at 1000 m depth. The absolute reference velocity at 1000 m for the observational study is based on Argo drift data at the parking depth of 1000 m [*Katsumata and Yoshinari*, 2010] and from the last 50 years of model velocity output at that depth for the model studies. The Scatterometer Climatology of Ocean Winds (SCOW) [*Risien and Chelton*, 2008] is used to compute the Ekman transport in the observational study, and the Ekman transport for each model is derived from the zonal wind stress output of the corresponding model.

The AMOC climatology estimated via the above methods in the models is validated against the direct calculation of the AMOC climatology from model velocity output. The differences in AMOC between the direct calculation and the indirect calculation from the model T/S fields are small, within ±0.6 Sv for both models. The AMOC estimates from the direct and indirect calculations also show very similar spatial and temporal characteristics to each other.
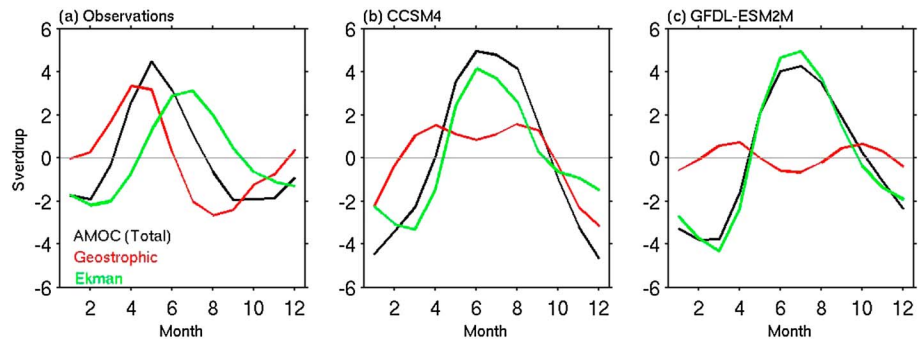
3. Time-Mean AMOC at 34°S

Following other studies [e.g., *Dong et al.*, 2009; *Kanzow et al.*, 2009], the AMOC in this study is defined as the maximum cumulative northward basin-wide volume transport in the upper water column. The mean AMOC at 34°S from Argo/WOA13 is approximately 18.4 Sv, similar to the mean value of 18.1 Sv obtained from XBT transects [*Dong et al.*, 2009; *Garzoli et al.*, 2013]. Results obtained here indicate that of the 18.4 Sv, 90% is contributed by the geostrophic transport (16.6 Sv) and the other 10% (1.8 Sv) is contributed by the Ekman transport. The mean AMOC determined from the model T/S fields is comparable with that from observations, 17.7 Sv for CCSM4 and 19.2 Sv for GFDL-ESM2M. Breaking up the mean AMOC transport into geostrophic and Ekman contributions shows that both the geostrophic (16.3 Sv) and Ekman (1.4 Sv) components from CCSM4 are slightly lower than, but close to, the observed estimates. The geostrophic transport from GFDL-ESM2M (16.2 Sv) is also slightly lower than the observed value. However, the Ekman transport from GFDL-ESM2M (3.0 Sv) is nearly twice as large as that estimated from satellite winds, which contributes to the stronger AMOC from this model.

Although the mean AMOC is well captured by the models, the zonal distribution of the geostrophic transport from models is quite different from that derived from the observations. The strong northward transport of 3°E, the eastern boundary current region, from the Argo/WOA13 observations (28.3 Sv) is not well represented in either model, with the mean transport values of 3°E of 14.9 Sv for CCSM4 and 10.4 Sv for GFDL-ESM2M. The southward transport of ~45°W (−24.5 Sv), the western boundary current region, is reasonably well captured by CCSM4 (−20.4 Sv), but not by GFDL-ESM2M (−5.8 Sv). In the interior region, the northward transport in CCSM4 (21.7 Sv) is too strong compared to the values from the Argo/WOA13 (12.9 Sv) and ESM2M (11.6 Sv). The Argo/WOA13-based estimates of the mean AMOC and boundary current contributions found herein are consistent with the previous values obtained from 17 quarterly high-density XBT transects carried out between 2002 and 2007 [*Dong et al.*, 2009].

4. Seasonal Cycle of AMOC at 34°S

The AMOC at 34°S estimated from both the observations and the models shows seasonal variations (Figure 1). However, their phase and amplitude, as well as contributions from the geostrophic and Ekman

Figure 1. Seasonal variations of the AMOC at 34°S (black) and contributions from the geostrophic (red) and Ekman (green) components estimated from (a) observations (Argo/WOA13 and SCOW) and two CMIP5 models, (b) CCSM4, and (c) GFDL-ESM2M. The time-mean values for the total AMOC and each component have been removed.

components, are different. We note that the time-mean values of transports were removed in Figure 1. The AMOC from observations reaches its maximum (22.9 Sv) in May and minimum (16.5 Sv) in September, with peak-to-peak amplitude of 6.4 Sv. Both the geostrophic and Ekman components contribute to the observed seasonal variations. The geostrophic transport has a peak-to-peak annual amplitude of 6.0 Sv, with the maximum in April (20.0 Sv) and the minimum in August (14.0 Sv). The Ekman transport peaks in July (4.9 Sv) and reaches its minimum in February (−0.4 Sv), yielding a slightly weaker peak-to-peak annual cycle of 5.3 Sv. The amplitudes of the observed Argo/WOA13 seasonal cycle in both the geostrophic and Ekman transports are consistent with those previously estimated from XBT transects [*Dong et al.*, 2009; *Garzoli et al.*, 2013], but the geostrophic transport computed from the XBTs peaks somewhat earlier than the results obtained from using the Argo/WOA13 data, in February instead of April. This small phase difference in the observed geostrophic transport may explain the weaker seasonal cycle of 1.8 Sv in the AMOC from the XBT transects [*Dong et al.*, 2009]. Also, the estimates from the XBT transects may be influenced by sampling aliasing in space and time [e.g., *Meinen et al.*, 2013], because the mean latitude of each transect varies slightly between 30°S and 35°S, and the transect is only sampled every 3 months. This suggests that more XBT realizations are needed to reduce the aliasing effect in the estimated annual cycle.

The AMOC from CCSM4 experiences a stronger total seasonal cycle (9.6 Sv), and its phase is shifted 1–3 months later than that found from the observational estimates, reaching its maximum in June and minimum in December. The result from GFDL-ESM2M also shows a stronger seasonal cycle in the AMOC (8.1 Sv), and its phase is shifted 2–5 months later than the observed values, with a maximum in July and a minimum in February. These phase differences illustrate the dominance of the Ekman transport in the modeled AMOC. In particular, the Ekman transport in the GFDL-ESM2M has a very strong seasonal peak-to-peak amplitude, 9.3 Sv, which is nearly twice the value estimated from the observed satellite winds. This strong seasonality in the modeled Ekman transport is directly linked to stronger seasonal variations in the zonal wind stress of the coupled models (not shown).

In contrast with the strong seasonal cycle in the observed geostrophic transport, both models exhibit seasonal variations in the geostrophic transports that are weaker than observed in the real ocean, particularly for GFDL-ESM2M (Figure 1). Both models also show semiannual variability that is absent from the observations, with peaks in April and October and troughs in January and July. This highlights a major problem that modern coupled models are having in reproducing the observed AMOC annual cycle, and we illustrate below that this is due to missing (or incorrect) physics in these coupled climate simulations.

To understand why the seasonal cycles in geostrophic transports are so different between the models and the observations, the vertical structure of the meridional velocity is examined. The distribution of zonally averaged geostrophic velocity from the observations shows vertically coherent seasonal variations (Figure 2), with anomalous northward flow from January to June and anomalous southward flow from July to December. This vertical coherence contributes to the strong seasonal cycle of the geostrophic transport in the upper ocean. In contrast, the zonally averaged geostrophic velocity from the model *T/S* climatologies do not exhibit this type of vertically coherent seasonal cycle. The geostrophic velocity within the surface mixed layer (<100 m) from both models shows a seasonal cycle with a maximum in April and a minimum in October, which is consistent with the mixed-layer velocity from observations. However, below the surface mixed
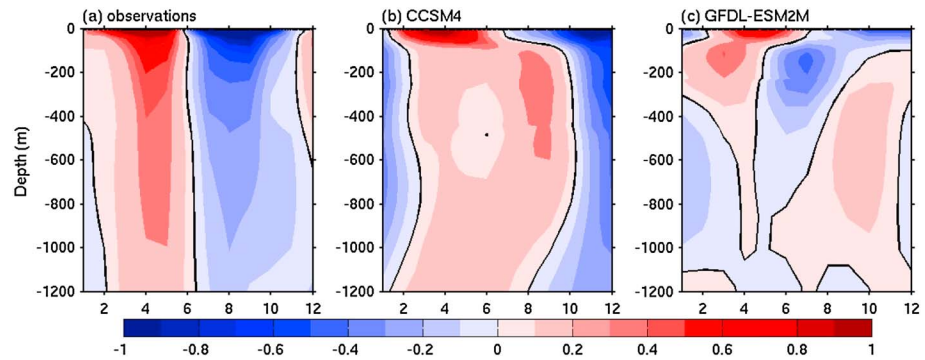
Figure 2. Month and depth distribution of zonally averaged meridional velocity along 34°S in the upper ocean computed from (a) observations and two CMIP5 models, (b) CCSM4, and (c) GFDL-ESM2M. The time-mean values at each depth have been removed to better demonstrate the seasonal variations. Units are in 10^{-3} m/s.

layer, the geostrophic velocity varies semiannually. Although different from the mixed-layer velocity, the subsurface velocity from CCSM4 is somewhat coherent, which peaks in August and troughs in December with a secondary trough in June. The different seasonality between the surface and subsurface geostrophic velocity results in the weakened seasonal variations of the total northward geostrophic transport in the upper water column and a superimposed weak semiannual signal. The vertical structure of the geostrophic velocity from GFDL-ESM2M is even more complex, and the phase of the annual and semiannual signal in the velocity varies with depth, resulting in essentially no annual signal and a weak semiannual signal in the geostrophic AMOC term.

The zonally averaged geostrophic velocity (or transport) at each depth is proportional to the dynamic height difference between the eastern and western boundaries, which is related to the density differences between the two boundaries. To understand why the models are producing erroneous vertical structures of geostrophic velocities throughout the annual cycle, it is therefore important to evaluate the annual cycle of the density field at the boundaries in both the observations and the models. The observed density in the surface mixed layer at both the eastern and western boundaries from Argo floats shows a similar seasonal cycle (Figures 3a and 3b) following the seasonal warming/cooling signals associated with the surface fluxes, although the amplitude is stronger, and the mixed layer is deeper at the western boundary. Below the surface mixed layer, the observed density at both boundaries shows vertically coherent seasonal variations, with the eastern boundary leading by 2 months. However, the density at the western boundary experiences relatively stronger seasonal variations. As a result, the observed east-west density differences are dominated by the density at the western boundary on the seasonal time scale (Figure 3c). This suggests that the western boundary plays a larger role in the seasonal variations of the observed geostrophic AMOC term at 34°S.

The density from the models (Figures 3d–3i) at both boundaries shows a similar seasonal cycle as observed from Argo in the surface mixed layer, although the mixed layer is shallower at the eastern boundary in the models compared to that observed by the Argo floats. Consistent with the observations, the western boundary also has a stronger control in the models on the density difference in the surface mixed layer. The subsurface densities at both boundaries in the models however strongly differ from the observations, and the eastern boundary plays an artificially large role in the east-west density differences in the models. Although the subsurface density at the western boundary from CCSM4 shows a vertically coherent seasonal cycle with positive anomalies during October to March and negative anomalies during April to September, these anomalies are almost exactly 180° out of phase with the seasonal cycle of the observed subsurface densities. The subsurface density signal at the eastern boundary in CCSM4 is even more complex (Figure 3e). Although the density experiences seasonal variations throughout the upper 1000 m, the phase of the seasonal cycle varies with depth, exhibiting sign reversals roughly every 400 m (e.g., between 200 m and 600 m and between 600 m and 1000 m). Further differentiating the CCSM4 results from the observations, the seasonal variation at the eastern boundary in CCSM4 is stronger than that at the western boundary, which explains its dominance of the subsurface east-west density difference in CCSM4.

The surface mixed layer in GFDL-ESM2M is very shallow (~20 m). Below the surface mixed layer down to 150 m depth, the density at both boundaries also shows strong seasonal variations (Figures 3g and 3h), but they are out of phase with the observed density seasonality (Figures 3a and 3b). The seasonal variations in the
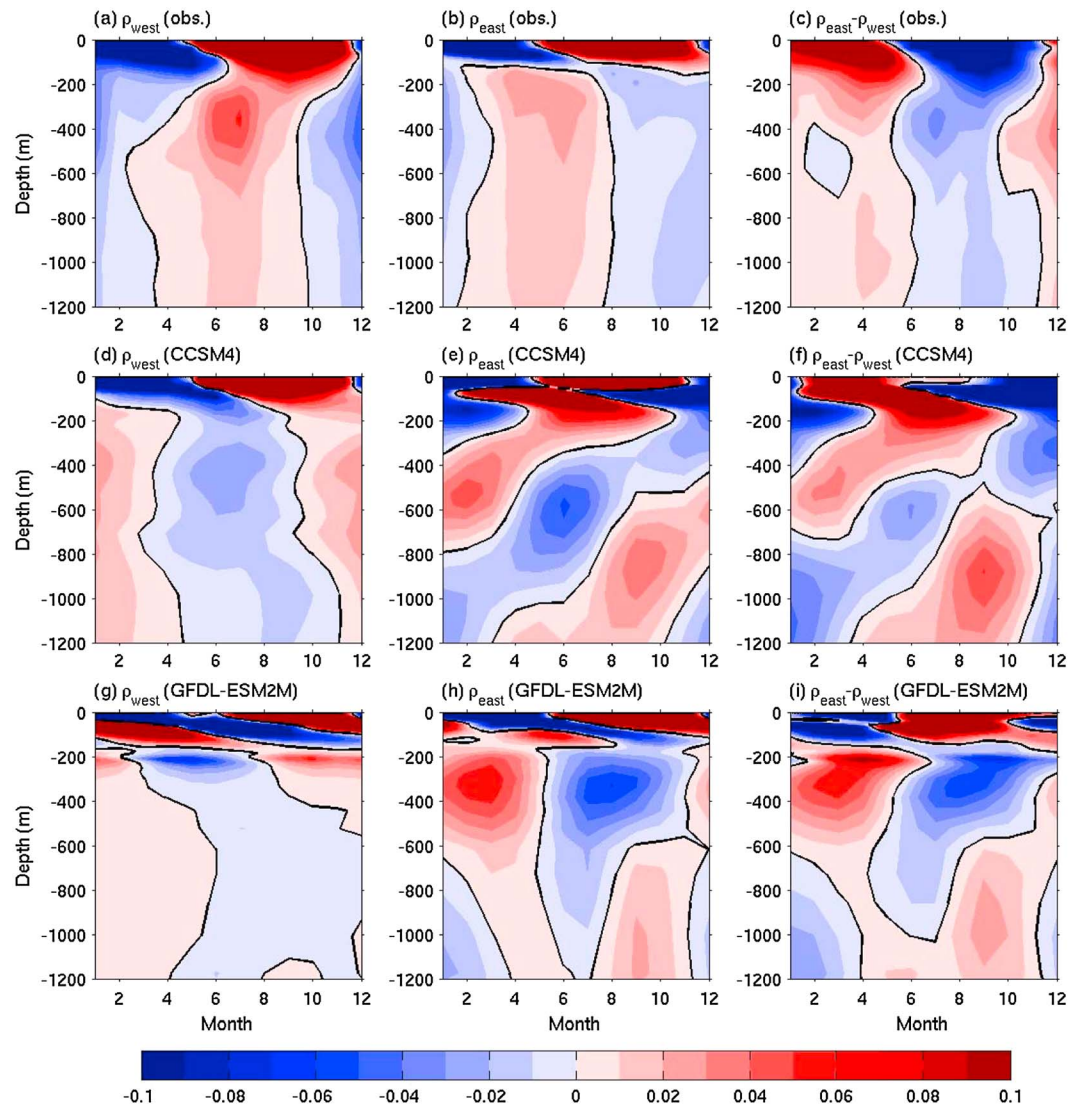
Figure 3. Water density at the (a) western and (b) eastern boundaries and (c) their differences (east minus west) from Argo climatology. (d–f) The same as Figures 3a–3c but from CCSM4 and (g–i) are from GFDL-ESM2M. As for Figure 2, the time-mean values at each depth have been removed. Units are in kg/m^3.

east-west density differences in GFDL-ESM2M are dominated by the variations at the western boundary in the upper 150 m. The seasonal cycle in density at the western boundary in the model is relatively weak below 150 m, and the variations in the density differences are controlled by the eastern boundary (unlike the observations). Similar to the CCSM4, the seasonal cycle of density at the eastern boundary is not vertically coherent, and the structure is complex.

These comparisons show that the disparity between the models and the observations may be the result of the model's inability to reproduce a realistic density annual cycle in the upper 1000 m of the water column at 34°S. The key objective then is to understand why the models are not producing the correct density variations.

5. Discussion

Wind stress curl at the eastern boundary has been thought to force the seasonal cycle of the AMOC at 26.5°N due to the strong control of density changes at the eastern boundary on the upper ocean transport [*Kanzow et al.*, 2010; *Chidichimo et al.*, 2010]. Similar to the North Atlantic, wind stress curl at the eastern boundary in the South Atlantic is much stronger and experiences a more substantial seasonal cycle than at
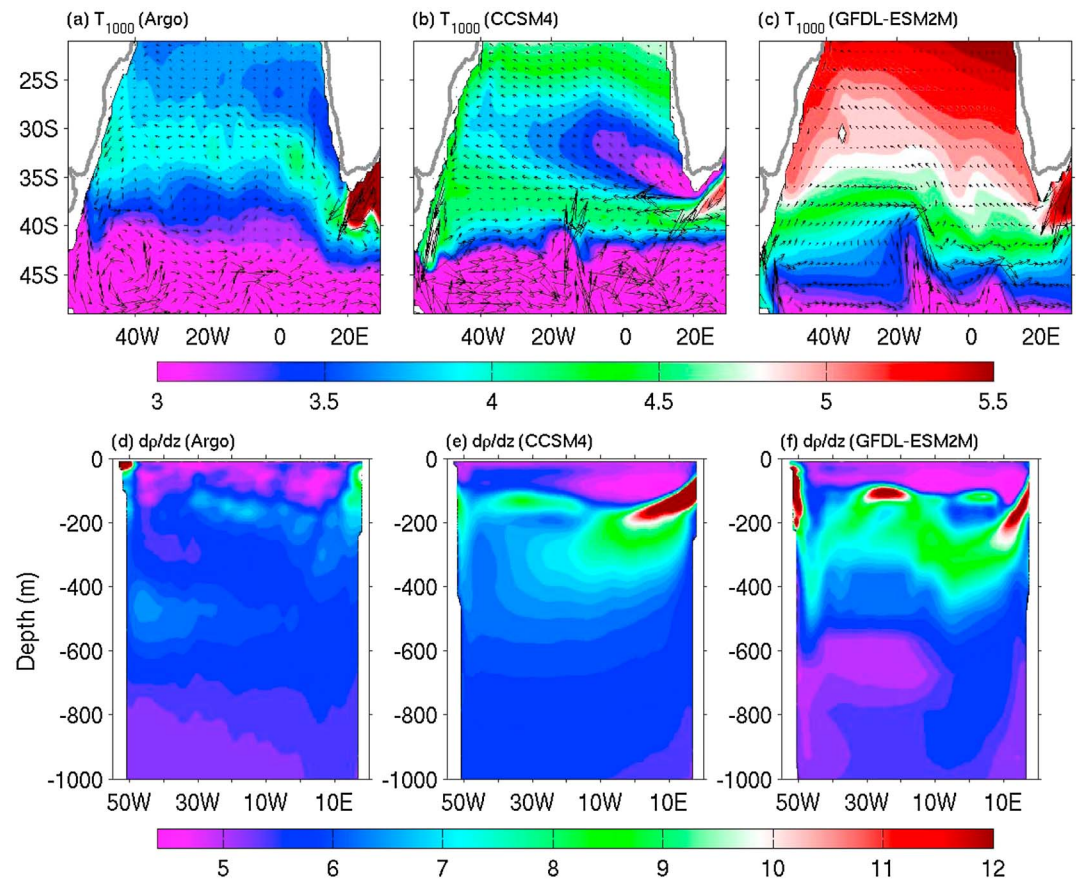
Figure 4. Time-mean temperature at 1000 m depth from (a) Argo data, (b) CCSM4, and (c) GFDL-ESM2M. The vectors show the current at the same depth. Vertical density gradient in the upper 1000 m for September derived from (d) Argo data, (e) CCSM4, and (f) GFDL-ESM2M. The distributions of vertical density gradient in other months are similar to Figures 4d–4f. September is used to avoid seasonal thermocline. Units for temperatures are in °C and in 10^{-3} kg/m^3 for density gradient.

the western boundary. Although the observations presented here indicate that eastern boundary plays a lesser role in the seasonal cycle of the geostrophic transport, the observed seasonal cycle of the density at the eastern boundary below the mixed layer is consistent with the local Ekman pumping effect from wind stress curl forcing, where positive density anomalies correspond to negative wind stress curl (upwelling) with about 3 month delay, and vice versa. The wind stress curl from the coupled models also shows a strong seasonal cycle at the eastern boundary, although it is out of phase with the observed winds (not shown). However, the Ekman pumping dynamics cannot explain the seasonality of the density in the upper 1000 m and its strong vertical incoherence in the models as compared to the real ocean.

While previous studies, conducted farther south, have shown that the Malvinas Current at the Confluence exhibits significant wind-forced annual and semiannual variability [*Goni and Wainer*, 2001; *Lentini et al.*, 2006; *Goni et al.*, 2011], at 34°S, the wind stress curl and its seasonal cycle at the western boundary are weak. Therefore, it is unlikely that local Ekman pumping plays a dominant role in the seasonal variation of the density in this region. Previous studies [e.g., *Matano et al.*, 1993; *Wainer et al.*, 2000; *Goni and Wainer*, 2001] found that the isotherms near the coast experience a stronger northward displacement during austral winter, when the northward flowing Malvinas Current is stronger and the southward flowing Brazil Current is weaker, and weaker displacement during austral summer, when the Malvinas Current is weaker and the Brazil Current is stronger. This seasonality of the currents is induced by the seasonal variations of the wind-driven gyre circulation [e.g., *Zhao and Johns*, 2014]. This is consistent with the observed positive density anomalies at the western boundary along 34°S during austral winter and negative anomalies during austral summer (Figure 3a). The northward extension of cold water (<4°C) can be seen at 1000 m depth from Argo data (Figure 4a). However, for reasons that are not completely clear, the Malvinas Current in the two

models turns to the east at around 40°S–42°S (Figures 4b and 4c), suggesting that it plays a minimal role in the temperature changes north of 40°S at the western boundary. This may explain the weak seasonality in density at the western boundary in the models. Besides their ineffectiveness in capturing the Malvinas Current, the general circulation pattern in the models largely differs from the observed current structure (Figure 4). For example, the westward propagation of warm water from the Agulhas Current system and cold water from the South Africa coast is not well represented, which clearly influences the basin-wide temperature distribution. The circulation pattern differences between the models and the observations explain some of the disagreements between the regional contributions to the mean AMOC discussed in section 3.

The strong baroclinicity at the base of the mixed layer in the model fields on both the western and eastern sides of the basin results in out-of-phase variations above and below this shear layer. This out-of-phase variation, particularly at the eastern boundary, contributes to the weaker seasonality in the modeled geostrophic transport below the mixed layer. This enhanced baroclinicity in the models is possibly due to the strong stratification in the modeled T/S fields. Examination of the monthly mean vertical density gradient (Figures 4d–4f) clearly shows the large model biases in the vertical stratification from 100 m to 500 m depth, particularly toward the eastern boundary. The strong stratification inhibits the models from transferring information from the mixed layer into the lower layers, resulting in the enhanced baroclinicity.

6. Conclusions

Observations suggest that the geostrophic transport plays an equal role to the Ekman transport in the AMOC seasonal variations at 34°S. This is different from the predominant control of the Ekman transport on the AMOC seasonality in the coupled climate models in the South Atlantic. Model biases in both the geostrophic and Ekman transports contribute to this difference. Compared to the observations, the models show stronger seasonal cycles in the Ekman transport and weaker seasonal cycles in the geostrophic transport.

The difference in geostrophic transports between the observations and the coupled models explains more of the disparity in the AMOC seasonal cycles between the models and the real world. The net geostrophic transport in the upper ocean across a transbasin section is related to the density difference between the eastern and western boundaries. The observed east-west density difference is largely controlled by the western boundary, whereas in the coupled models, the eastern boundary dominates. The observed seasonal cycle of the density at the western boundary is controlled by the strength of the Malvinas Current, which induces a considerable northward excursion of the coastal isotherms during winter when it is strong. In the models, however, the Malvinas Current plays a minimal role in the density changes at the western boundary because it separates from the coast farther south, allowing the eastern boundary to dominate. The other factor behind the strong seasonal cycle in the geostrophic transport from the observations is associated with the vertical coherence in the velocity signals below the mixed layer. The models lack this vertical coherence, showing strong baroclinicity below the surface mixed layer, yielding out-of-phase variations that sum to a very weak annual cycle in the geostrophic transports in the models. Evaluating the vertical density gradients in both the data and the models suggests that the structure in the models below the mixed layer is likely due to erroneously strong vertical density shear, which prevents the models from correctly moving information down from the mixed layer to the deeper layers.

References

Baringer, M. O., et al. (2013), Meridional Overturning Circulation and heat transport observations in the Atlantic Ocean, in "State of the Climate in 2012", *Bull. Am. Meteorol. Soc.*, *94*(8), S65–S68.

Böning, C. W., C. Dieterich, B. Barnier, and Y. L. Jia (2001), Seasonal cycle of the meridional heat transport in the subtropical North Atlantic: A model intercomparison in relation to observations near 25°N, *Prog. Oceanogr.*, *48*, 231–253.

Chidichimo, M. P., T. Kanzow, S. A. Cunningham, W. E. Johns, and J. Marotzke (2010), The contribution of eastern-boundary density variations to the Atlantic Meridional Overturning Circulation at 26.5°N, *Ocean Sci.*, *6*, 475–490, doi:10.5194/os-6-475-2010.

Danabasoglu, G., S. G. Yeager, Y.-O. Kwon, J. J. Tribbia, A. S. Phillips, and J. W. Hurrell (2012), Variability of the Atlantic Meridional Overturning Circulation in CCSM4, *J. Clim.*, *25*, 5153–5172, doi:10.1175/JCLI-D-11-00463.1.

Dong, S., S. L. Garzoli, M. O. Baringer, C. S. Meinen, and G. J. Goni (2009), Interannual variations in the Atlantic Meridional Overturning Circulation and its relationship with the net northward heat transport in the South Atlantic, *Geophys. Res. Lett.*, *36*, L20606, doi:10.1029/2009GL039356.

Dong, S., M. O. Baringer, G. J. Goni, and S. L. Garzoli (2011), Importance of the assimilation of Argo float measurements on the Meridional Overturning Circulation in the South Atlantic, *Geophys. Res. Lett.*, *38*, L18603, doi:10.1029/2011GL048982.

Dunne, J. P., et al. (2012), GFDL's ESM2 Global Coupled Climate–Carbon Earth System Models. Part I: Physical formulation and baseline simulation characteristics, *J. Clim.*, *25*, 6646–6665.

Garzoli, S. L., and M. O. Baringer (2007), Meridional heat transport determined with expendable bathythermographs, Part II: South Atlantic transport, *Deep-Sea Res., Part I*, *54*(8), 1402–1420.

Garzoli, S. L., M. O. Baringer, S. Dong, R. C. Perez, and Q. Yao (2013), South Atlantic meridional fluxes, *Deep Sea Res., Part I*, *71*, 21–32, doi:10.1016/j.dsr.2012.09.003.

Gent, P. R., et al. (2011), The Community Climate System Model version 4, *J. Clim.*, *24*, 4973–4991, doi:10.1175/2011JCLI4083.1.

Goni, G. J., and I. Wainer (2001), Investigation of the Brazil Current front variability from altimeter data, *J. Geophys. Res.*, *106*, 31,117–31,128.

Goni, G. J., F. Bringas, and P. N. Di Nezio (2011), Observed low frequency variability of the Brazil Current front, *J. Geophys. Res.*, *116*, C10037, doi:10.1029/2011JC007198.

Jayne, S. R., and J. Marotzke (2001), The dynamics of ocean heat transport variability, *Rev. Geophys.*, *39*, 385–411.

Johns, W. E., et al. (2011), Continuous, array-based estimates of Atlantic Ocean heat transport at 26.5°N, *J. Clim.*, *24*, 2429–2449.

Kanzow, T., H. Johnson, D. Marshall, S. A. Cunningham, J. J.-M. Hirschi, A. Mujahid, H. L. Bryden, and W. E. Johns (2009), Basinwide integrated volume transports in an eddy-filled ocean, *J. Phys. Oceanogr.*, *39*, 3091–3110.

Kanzow, T., et al. (2010), Seasonal variability of the Atlantic Meridional Overturning Circulation at 26.5°N, *J. Clim.*, *23*, 5678–5698.

Katsumata, K., and H. Yoshinari (2010), Uncertainties in global mapping of Argo drift data at the parking level, *J. Oceanogr.*, *66*, 553–569.

Lentini, C., G. Goni, and D. Olson (2006), Investigation of Brazil Current rings in the confluence region, *J. Geophys. Res.*, *111*, C06013, doi:10.1029/2005JC002988.

Locarnini, R. A., and et al. (2013), *World Ocean Atlas 2013, Volume 1: Temperature*, S. Levitus, and A. Mishonov, NOAA Atlas NESDIS 73, 40 pp., NOAA, Silver Spring, Md.

Matano, R. P., M. G. Schlax, and D. B. Chelton (1993), Seasonal variability in the South Atlantic, *J. Geophys. Res.*, *98*, 18,027–18,035.

McCarthy, G., and et al. (2012), Observed interannual variability of the Atlantic Meridional Overturning Circulation at 26.5°N, *Geophys. Res. Lett.*, *39*, L19609, doi:10.1029/2012GL052933.

Meinen, C. S., S. Speich, R. C. Perez, S. Dong, A. R. Piola, S. L. Garzoli, M. O. Baringer, S. Gladyshev, and E. J. D. Campos (2013), Temporal variability of the Meridional Overturning Circulation at 34.5°S: Results from two pilot boundary arrays in the South Atlantic, *J. Geophys. Res. Oceans*, *118*, 6461–6478, doi:10.1002/2013JC009228.

Msadek, R., W. E. Johns, S. G. Yeager, G. Danabasoglu, T. L. Delworth, and A. Rosati (2013), The Atlantic meridional heat transport at 26.5°N and its relationship with the MOC in the RAPID array and the GFDL and NCAR coupled models, *J. Clim.*, *26*, 4335–4356, doi:10.1175/JCLI-D-12-00081.1.

Parsons, L. A., J. Yin, J. T. Overpeck, R. J. Stouffer, and S. Malyshev (2014), Influence of the Atlantic Meridional Overturning Circulation on the monsoon rainfall and carbon balance of the American tropics, *Geophys. Res. Lett.*, *41*, 146–151, doi:10.1002/2013GL058454.

Risien, C. M., and D. B. Chelton (2008), A global climatology of surface wind and wind stress fields from eight years of QuikSCAT scatterometer data, *J. Phys. Oceanogr.*, *38*, 2379–2413.

Roemmich, D., and J. Gilson (2009), The 2004–2008 mean and annual cycle of temperature, salinity, and steric height in the global ocean from the Argo Program, *Prog. Oceanogr.*, *82*, 81–100.

Smith, R. S., and J. M. Gregory (2009), A study of the sensitivity of ocean overturning circulation and climate to freshwater input in different regions of the North Atlantic, *Geophys. Res. Lett.*, *36*, L15701, doi:10.1029/2009GL038607.

Stouffer, R. J., J. Yin, and J. M. Gregory (2006), Investigating the causes of the response of the thermohaline circulation to past and future climate changes, *J. Clim.*, *19*(8), 1365–1387.

Thorpe, R. B., J. M. Gregory, T. C. Johns, R. A. Wood, and J. F. B. Mitchell (2001), Mechanisms determining the Atlantic thermohaline circulation response to greenhouse gas forcing in a non-flux-adjusted coupled climate model, *J. Clim.*, *14*, 3102–3116.

Vellinga, M., and R. A. Wood (2002), Global climatic impacts of a collapse of the Atlantic thermohaline circulation, *Clim. Change*, *54*(3), 251–267.

Wainer, I., P. Gent, and G. Goni (2000), Annual cycle of the Brazil-Malvinas Confluence region in the National Center for Atmospheric Research climate system model, *J. Geophys. Res.*, *105*, 26,167–26,177, doi:10.1029/1999JC000134.

Zhang, R., and T. L. Delworth (2006), Impact of Atlantic multidecadal oscillations on India/Sahel rainfall and Atlantic hurricanes, *Geophys. Res. Lett.*, *33*, L17712, doi:10.1029/2006GL026267.

Zhao, J., and W. Johns (2014), Wind-Driven seasonal cycle of the Atlantic Meridional Overturning Circulation, *J. Phys. Oceanogr.*, *44*, 1541–1562.